
Sonicmesh: Enhancing 3D Human Mesh Reconstruction in Vision-Impaired Environments With Acoustic Signals

Xiaoxuan Liang^{*1} Wuyang Zhang^{*1} Hong Zhou² Zhaolong Wei¹ Sicheng Zhu³ Yansong Li⁴ Rui Yin³
Jiantao Yuan³ Jeremy Gummeson¹

Abstract

3D Human Mesh Reconstruction (HMR) from 2D RGB images faces challenges in environments with poor lighting, privacy concerns, or occlusions. These weaknesses of RGB imaging can be complemented by acoustic signals, which are widely available, easy to deploy, and capable of penetrating obstacles. However, no existing methods effectively combine acoustic signals with RGB images for robust 3D HMR. The primary challenges include the low-resolution images generated by acoustic signals and the lack of dedicated processing backbones. We introduce SonicMesh, a novel approach combining acoustic signals with RGB images to reconstruct 3D human mesh. To address the challenges of low resolution and the absence of dedicated processing backbones in images generated by acoustic signals, we modify an existing method, HRNet, for effective feature extraction. We also integrate a universal feature embedding technique to enhance the precision of cross-dimensional feature alignment, enabling SonicMesh to achieve high accuracy. Experimental results demonstrate that SonicMesh accurately reconstructs 3D human mesh in challenging environments such as occlusions, non-line-of-sight scenarios, and poor lighting.

as the inherent ambiguity in inferring depth information from 2D images in computer vision. Without a complete 3D mesh, applications like AR/VR (Tang et al., 2021), human pose estimation (Fang et al., 2017; Zheng et al., 2022), and human-computer interaction (Ryselis et al., 2020) become infeasible. Traditional Human Mesh Reconstruction (HMR) methods encounter challenges with occlusions and low visibility, resulting in inaccuracies. Recent works have explored alternative sensing technologies to enhance camera capabilities (Zhao et al., 2019), including mmWave (Xue et al., 2021; Chen et al., 2022), Radio Frequency (RF) (Geng et al., 2022; Zhao et al., 2019), and LiDAR (Li et al., 2022; Bai et al., 2022). However, these methods have limitations, such as high costs, specialized hardware requirements, and significant power consumption.

In contrast, acoustic signals provide millimeter-level positioning accuracy (Li et al., 2020), cost-effectiveness, and ease of deployment. Techniques such as Synthetic Aperture Radar (SAR) (Mao et al., 2018) use acoustic signals for object imaging, while others utilize phase changes in echoes for gesture recognition (Li et al., 2020). In addition to enhanced privacy, acoustic signals operate effectively under various visibility conditions, making it a valuable method for improving human mesh reconstruction in computer vision. Therefore, Acoustic signals offer a promising alternative for HMR using only RGB images. Also, they are widely available, easy to deploy, and capable of penetrating obstacles.

However, to the best of our knowledge, no existing methods have successfully reconstructed a complete 3D mesh of the human body using only acoustic signals due to challenges such as environmental noise, signal attenuation, and weak echo signals¹. Also, images generated by acoustic signals (Liang et al., 2024) have a low resolution. Therefore, to overcome the limitations of both methods, methods that combine RGB images with acoustic signals for 3D Human Mesh Reconstruction (HMR) are needed.

¹Acoustic sensing typically requires frequencies above 16 kHz to capture fine details, which results in significant signal loss and limits resolution.

1. Introduction

Recovering a complete 3D mesh of human bodies from fragmented RGB data is challenging. Data can be compromised by issues such as occlusions, where parts of the body are hidden from view, and variations in body poses and shapes across individuals. Additional complications include the complexity of clothing and accessories, as well

^{*}Equal contribution ¹University of Massachusetts at Amherst, Location, Country ²Trine University ³Zhejiang University ⁴University of Illinois at Chicago. Correspondence to: Jeremy Gummeson <jgummeso@umass.edu>.

To combine RGB images with acoustic signals for 3D HMR, previous works (Wang et al., 2023; Zhao et al., 2019; Xue et al., 2021; Shibata et al., 2023; Zhao et al., 2019; Yang et al., 2022b; Chen et al., 2023) hand-craft features from signals and use them to reconstruct 3D meshes. For instance, Wang et al. (2023) uses Angle of Arrival (AoA) to visualize the 3D mesh from RF signals, but this approach risks losing detail due to reliance on predefined features.

In contrast, we develop *SonicMesh*, an end-to-end HMR method that leverages RGB images and acoustic signals to directly output 3D meshes without relying on any predefined features. SonicMesh converts acoustic signals into images, preserving data integrity before fusing them with RGB images. Although Transformer models support multimodal fusion (Wang et al., 2022c; Bai et al., 2022; Chen et al., 2023; Wang et al., 2022d), there is a lack of systems specifically designed for fusing acoustic and RGB images. SonicMesh also addresses this gap by leveraging the unique characteristics of both acoustic and visual data, enhancing feature integration and model performance. SonicMesh employs a modified HRNet (Sun et al., 2019) backbone to extract features from images generated by acoustic signals, which are combined with RGB images to create a comprehensive global feature set. This set is processed by a custom-designed Transformer, effectively fusing both data types to achieve accurate 3D human mesh reconstruction. In summary, our contributions are:

- We introduce SonicMesh, the first method for 3D human body reconstruction based on acoustic-RGB fusion without predefined features.
- We propose a registration module that utilizes feature embeddings from both acoustic and RGB data that improve 3D mesh reconstruction accuracy.
- We modify HRNet to improve feature extraction from acoustic signals. The modified HRNet achieves high resolution.

2. Related works

This section provides an overview of state-of-the-art (SOTA) studies relevant to our work.

3D human mesh reconstruction 3D HMR is essential in computer vision and graphics, creating 3D models of human bodies from inputs like images, videos, or depth data. Techniques for 3D reconstruction from RGB images are categorized into parametric (Loper et al., 2023) and non-parametric (Lin et al., 2021b) methods. The parametric approach, such as the Skinned Multi-Person Linear (Loper et al., 2023) (SMPL) model, uses predefined body parameters to generate the mesh. Non-parametric methods, like

the METRO (Lin et al., 2021b) system, directly compute mesh vertices from images using transformer encoders to manage vertex-vertex and vertex-joint interactions, producing 3D joint coordinates and mesh vertices simultaneously. Researchers are also exploring alternative data sources to improve 3D reconstruction under various conditions. For example, Chen et al. introduced ImmFusion (Chen et al., 2023), which combines mmWave and RGB data to reconstruct 3D human bodies in all weather conditions. Similarly, Zhao et al. developed RF-Avatar (Zhao et al., 2019), using radio frequency signals in the WiFi range to estimate 3D human meshes, effective in occluded environments.

Acoustic sensing Acoustic sensing is widely used due to its integration into affordable, accessible devices like smartphones. It is particularly effective for precise distance estimation due to sound’s slow propagation speed. For example, CAT (Mao et al., 2016) and Rabbit (Mao et al., 2017) systems use acoustic-FMCW (Frequency Modulated Continuous Wave) signals to estimate distances by measuring frequency differences between transmitted signals and echoes. The Acousticcardiogram (Qian et al., 2018) (ACG) system applies this principle to monitor health by detecting chest movements from heartbeats and breathing. The AcuTe (Cai et al., 2020) system estimates temperature by calculating propagation delays, as temperature affects sound speed. In more complex applications, Shibata et al. (2023) proposed a 3D human pose estimation system using two loudspeakers and an ambisonics microphone, though this setup is not feasible for commercial devices like smartphones. Additionally, using acoustic signal features in neural networks complicates the learning process and can reduce result reliability. In summary, our work demonstrates effective human body detection using acoustic signals on commercial devices.

3. Images generated by acoustic signal

In this section, we discuss methods for generating 2D images from acoustic signals in 3D spaces. Throughout the paper, we use the term “*acoustic images*” to denote these 2D images. We employ a technology, Inverse Synthetic Aperture Radar (ISAR)-based imaging, originally developed for military applications, such as capturing the shapes of objects like planes and ships, which has now been adapted for hand gesture recognition through acoustic images (Wang et al., 2022b; Liang et al., 2024). ISAR-based imaging achieves this by considering multiple scatter points (Unlike motion tracking, which treats a moving target as a single scatter point). ISAR converts the target’s translational motion into rotational motion and synthesizes reflected signals from various angles.

To capture reflections, we generate a Linear Frequency Modulation (LFM) waveform between 18kHz and 22kHz, utiliz-

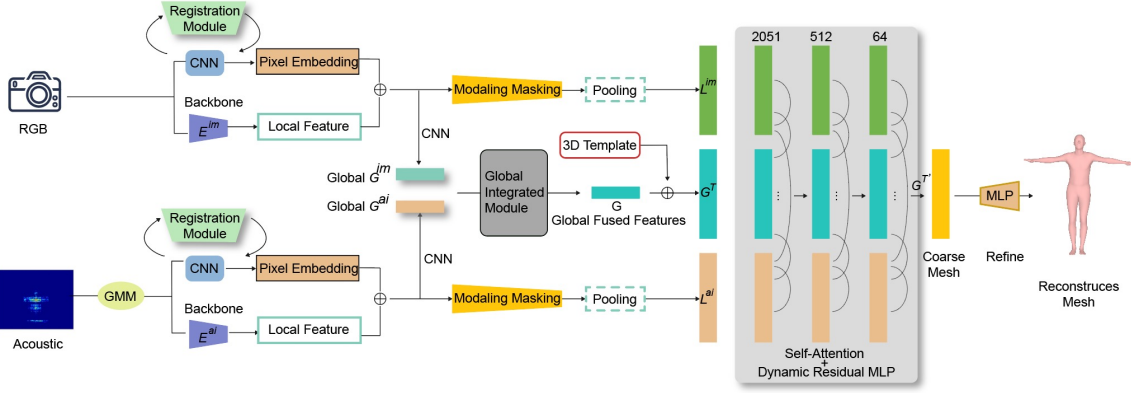


Figure 1. The architecture of SonicMesh.

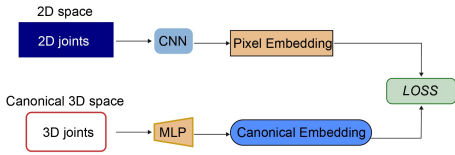


Figure 2. The illustration of Registration Module.

ing omnidirectional microphones and a speaker to simultaneously transmit and receive acoustic signals in 3D spaces. Once the echo signals are received, a bandpass filter in the 18-22kHz range extracts the chirp signals, ensuring we capture only the relevant frequencies. To further refine the data, we use background subtraction to eliminate direct path and multi-path reflections, operating under the assumption of a static background. However, when the target moves, time delays are introduced in the reflected signals, complicating the acquisition process. To address this, we align echo signals across profiles to synchronize any delays caused by movement. After achieving alignment, we multiply the echo signal by the transmitted chirps, down-converting the samples and storing them as a 2D data matrix, referred to as intermediate-frequency (IF) signals. Next, to correct any phase offsets that arise from the alignment process, we apply the Minimum Entropy Autofocus (MEA) algorithm (Chen et al., 2017), a method commonly used in radar imaging. Finally, a 2D FFT is performed on the IF signal matrix to generate the target image, completing the reconstruction process. More technical details about the acoustic image generating process are discussed in Sec. A.

4. Architecture of SonicMesh

This section presents the architecture and key components of SonicMesh; our framework for human mesh reconstruction uses acoustic-RGB fusion. We begin by introducing our

Registration Module (Sec. 4.1), designed to align features in RGB and acoustic images for accurate pose estimation. Next, we describe our *enhanced acoustic feature detection* approach (Sec. 4.2), which overcomes the challenges associated with processing low-resolution acoustic images. This section then presents our *transformer-based fusion* mechanism (Sec. 4.3), which combines global and local features from both RGB and acoustic images to form comprehensive body representations. Finally, we describe our techniques for masking and integrating different input types (Sec. 4.4), designed to ensure robust performance even when the quality varies between RGB and acoustic images.

SonicMesh’s pipeline (Fig. 1) consists of three main stages. First, specialized Convolutional Neural Networks extract pixel embeddings and local features from both acoustic and RGB images, capturing essential characteristics like texture, edges, and spatial relationships. Next, these features undergo cross-modal registration and enhancement, where acoustic features are refined to align the detail level of RGB features. Finally, our transformer-based fusion module combines these processed features to generate an accurate 3D human mesh while preserving natural joint constraints, body proportions, and physical limitations of human anatomy. We achieve this by using SMPL-X (Pavlakos et al., 2019) template, the details on can be found in Appendix B.1

SonicMesh effectively leverages the complementary strengths of both RGB and acoustic images - the depth perception and obstacle penetration of acoustic signals, alongside the high-resolution surface details of RGB images - enabling robust reconstruction across various challenging scenarios.

4.1. Registration Module

While SMPL-X provides a parametric template for human body modeling, accurately mapping features from RGB

and acoustic images to this template remains challenging. Features such as human skeletons are lost in the SMPL-X template (more discussions in Appendix B.1). Current methods (Chen et al., 2023) resolve the issue using generic backbones to extract and combine features from both acoustic and RGB images (Qi et al., 2017; Fan et al., 2021; Wang et al., 2022a). However, while these approaches effectively capture *low-level features* (signal characteristics and image textures), they also fail to preserve crucial *high-level features* (structural information), such as the skeletal joint configurations.

To address feature loss in 3D mesh reconstruction using 2D acoustic and RGB images, we introduce a Registration Module (RM) in SonicMesh that aligns 2D features with canonical 3D embeddings (Yang et al., 2022a). RM operates on both 2D RGB and acoustic images (Section 3).

The registration process begins by identifying 16 anatomical keypoints projected onto the 2D image, represented as a set of joints $\mathbf{J}^a = \{\mathbf{k}_j^a\}_{j=1}^J$, where each $\mathbf{k}_j^a \in \mathbb{R}^2$ denotes the (x, y) coordinates of the j -th joint and $J = 16$ is the feature dimension. These keypoints include critical anatomical landmarks such as the head, shoulders, elbows, wrists, hips, knees, ankles, and spine points (shown in Fig. 7, Sec. C.2).

For each projected joint \mathbf{k}_j^a , a Convolutional Neural Network (CNN) ψ^a extracts initial 2D feature embeddings:

$$\psi^a(\mathbf{k}_j^a) = \text{CNN}_{\psi^a}(\mathbf{k}_j^a), \quad (1)$$

where $\psi^a(\mathbf{k}_j^a) \in \mathbb{R}^{16}$ represents a collective embedding capturing spatial relationships and local characteristics of all anatomical joints in 2D space. After feature fusion with the 3D template, a second registration stage ϕ^a maps these fused features to their corresponding 3D locations:

$$\phi^a(\psi^a(\mathbf{k}_j^a), T) = \text{MLP}_{\phi^a}(\psi^a(\mathbf{k}_j^a), T), \quad (2)$$

where T represents the 3D SMPL-X template features. This two-stage registration ensures both accurate 2D feature alignment and proper 3D spatial correspondence, enabling anatomically consistent mesh reconstruction, as illustrated in Fig. 2.

For processing 3D joint information, we employ a Multi-Layer Perceptron (MLP) rather than a CNN, as 3D point coordinates lack the grid-like structure that CNNs are designed to handle. We denote all joints in 3D canonical space as a set $\mathbf{J}^* = \{\mathbf{K}_i^*\}_{i=1}^J$, where each $\mathbf{K}_i^* \in \mathbb{R}^3$ represents the (x, y, z) coordinates of the i -th joint. The MLP extracts joint features as:

$$\psi(\mathbf{K}_i^*) = \text{MLP}_{\psi}(\mathbf{K}_i^*) \quad (3)$$

where $\psi(\mathbf{K}_i^*) \in \mathbb{R}^{16}$ produces a feature embedding in the same space as the 2D features from Eq. 1.

Having established parallel feature embeddings in both 2D and 3D space, we now need a mechanism to align these features accurately. We employ a soft argmax descriptor matching technique to compute the corresponding 3D joint coordinates $\hat{\mathbf{K}}_j^*$ in canonical space (Yang et al., 2022a):

$$\hat{\mathbf{K}}_j^* = \sum_{\mathbf{K} \in \mathbf{V}^*} s(\mathbf{k}_j^a) \mathbf{K}, \quad (4)$$

where \mathbf{V}^* represents sampled points in the canonical 3D grid. The normalization function s is defined as a softmax function that weights the contributions of different joint positions in 3D spaces, i.e.,

$$s(\mathbf{k}_j^a) = \text{softmax}\left(\left\{\left\langle \psi^a(\mathbf{k}_j^a), \psi(\mathbf{K}) \right\rangle\right\}_{\mathbf{K} \in \mathbf{V}^*}\right), \quad (5)$$

where $\langle \cdot, \cdot \rangle$ is the cosine similarity between feature embeddings, enabling us to identify the most possible aligned 3D position for each 2D joint by comparing their feature representations. More discussion of using soft argmax functions are discussed in Appendix B.3.

To evaluate and optimize the alignment between predicted 3D points and their corresponding 2D embeddings, we introduce a feature matching loss:

$$\mathcal{L}_{\text{match}} = \sum_{\mathbf{k}_j^a} \left\| \hat{\mathbf{K}}^*(\mathbf{k}_j^a) - \mathbf{K}^*(\mathbf{k}_j^a) \right\|_2^2, \quad (6)$$

where $\mathcal{L}_{\text{match}}$ measures the squared Euclidean distance between predicted 3D coordinates $\hat{\mathbf{K}}^*$ and ground truth (captured using a calibrated camera system, more details in Sec. 5.1) coordinates \mathbf{K}^* for each joint \mathbf{k}_j^a , minimizing $\mathcal{L}_{\text{match}}$ ensures predicted positions closely match the true ones, enhancing 3D reconstruction accuracy.

While these alignment techniques establish correspondence between 2D and 3D features, acoustic-generated images present additional challenges due to their inherently low resolution and reduced clarity compared to RGB images. These limitations stem from the physical properties of acoustic signal propagation and reflection. To address these challenges, we introduce enhanced feature detection techniques in Sec 4.2.

4.2. Enhanced acoustic feature detection

As shown in the Ground Truth and Acoustic Image columns in Fig. 3, acoustic images often suffer from low resolution (more discussions in Appendix A.1). To address these challenges, we propose a two-stage approach combining segmentation and localization techniques.

First, we employ Fast-CNN (Girshick, 2015) to detect human figures in acoustic images. Fast-CNN uses a bounding-box technique to efficiently scan acoustic images, identifying regions where shape and intensity patterns suggest

human presence. This initial detection stage provides coarse spatial localization of human figures within the acoustic image.

Second, to achieve more precise pose detection, we employ a Gaussian Mixture Model (GMM) within the detected regions. GMM is particularly well-suited for this refinement task, because GMM effectively handles the inherent noise and uncertainty in acoustic data, models the natural clustering of human body parts, and captures the spatial relationships between different body segments. This two-stage approach enables robust human pose detection despite the low-resolution nature of acoustic images.

Using GMM, the human body within the bounding boxes provided by Fast-CNN is further segmented into distinct regions based on the pose. We then identify 16 key joint points to reconstruct the human pose, with each joint point constrained to its corresponding segmented region as defined by the GMM. To locate each joint, we calculate the geometric center of each segment, $\bar{x} \triangleq \sum_{i=1}^N x_i/N$, where x_i are points within a segment and N is the total number of points in the segment, and analyze areas of maximal density as potential joint locations. This selection focuses on intersections and peripheries of these segments, minimizing the Euclidean distance $d(\mathbf{p}, \mathbf{q}) \triangleq \sqrt{\sum_{i=1}^N (q_i - p_i)^2}$ between centroids \mathbf{p} and \mathbf{q} of adjacent segments, as well as density measurements to identify clusters of data points within each segment.

Having established methods for both aligning 2D-3D features and enhancing acoustic image quality, we next present our approach for fusing RGB and acoustic information to create comprehensive 3D human mesh reconstructions.

4.3. Transformer fusion with global and local features

In this subsection, we present our feature fusion framework that integrates global and local features (discussed in Sec. 4.1 and App. B.2) from both RGB and acoustic images to form a comprehensive body representation.

Starting with RGB and acoustic images (generated as described in Section 3), we use HRNet (Sun et al., 2019) as our backbone to extract initial features $F = \text{HRNet}(I)$. These features then undergo two transformations: a pixel embedding mapping ϕ (Bai et al., 2022) that transforms features into a higher-dimensional vector $V = \phi(F)$, followed by a 3D projection function ψ (Bai et al., 2022) that maps these features into 3D space.

From the enhanced feature space $\psi(V)$, our framework extracts complementary features at two scales:

$$G = \text{CNN}(V), \quad L = \text{Pool}(\text{Mask}(V)), \quad (7)$$

where global features G (comprising G^{im} and G^{ai} from RGB and acoustic images) capture overall body structure

through CNN layers, while local features L (comprising L^{im} and L^{ai}) preserve fine-grained anatomical details through masked pooling operations (More details in App. B.2).

This dual-scale approach ensures both global coherence through complete body configuration and inter-limb relationships, as well as local precision through detailed joint and boundary features. The combination of both feature scales enables accurate reconstruction of the complete 3D mesh while maintaining structural integrity and anatomical detail.

To achieve the final reconstruction, we must effectively combine complementary information from multiple sources: RGB images (providing texture but lacking depth), acoustic images (offering depth at lower resolution), and a predefined SMPL-X template T defined in Sec. 4.1 (ensuring anatomical consistency).

Our feature integration process occurs in two stages. First, we use a Global Integrated Module to normalize and combine features from different modalities:

$$G^T = f(G^{\text{im}}, G^{\text{ai}}, T), \quad (8)$$

where G^T represents a unified feature set that incorporates RGB textures, acoustic depth cues, and template-based constraints from SMPL-X (details in Appendix C).

Building on this global representation, we then integrate local features using a multi-head transformer ϕ_L :

$$M = \phi_L(G^T, L^{\text{ai}}, L^{\text{im}}), \quad (9)$$

The transformer uses self-attention mechanisms to identify and prioritize important feature interactions across modalities, while MLPs reduce dimensionality to create M , the final mesh-ready feature set. This two-stage approach ensures that both global structure and local details are preserved in the final reconstruction.

4.4. Modality masking and global integrated module

Reliable 3D human mesh reconstruction requires consistent performance across diverse environments. While RGB and acoustic signals offer complementary strengths - RGB providing detailed features in good lighting and acoustic signals excelling in low visibility - naively combining these modalities creates a critical challenge. During training, models naturally gravitate toward the higher-quality RGB features in well-lit conditions (Bijelic et al., 2020; Chen et al., 2023). This bias manifests in two ways: the model fails to fully leverage acoustic signals when they would be most valuable (such as in poor lighting or occlusions), and simultaneously becomes overly reliant on RGB data quality, making the system vulnerable to environmental variations.

Understanding this fundamental challenge motivates our key technical contribution: strategies to enforce balanced

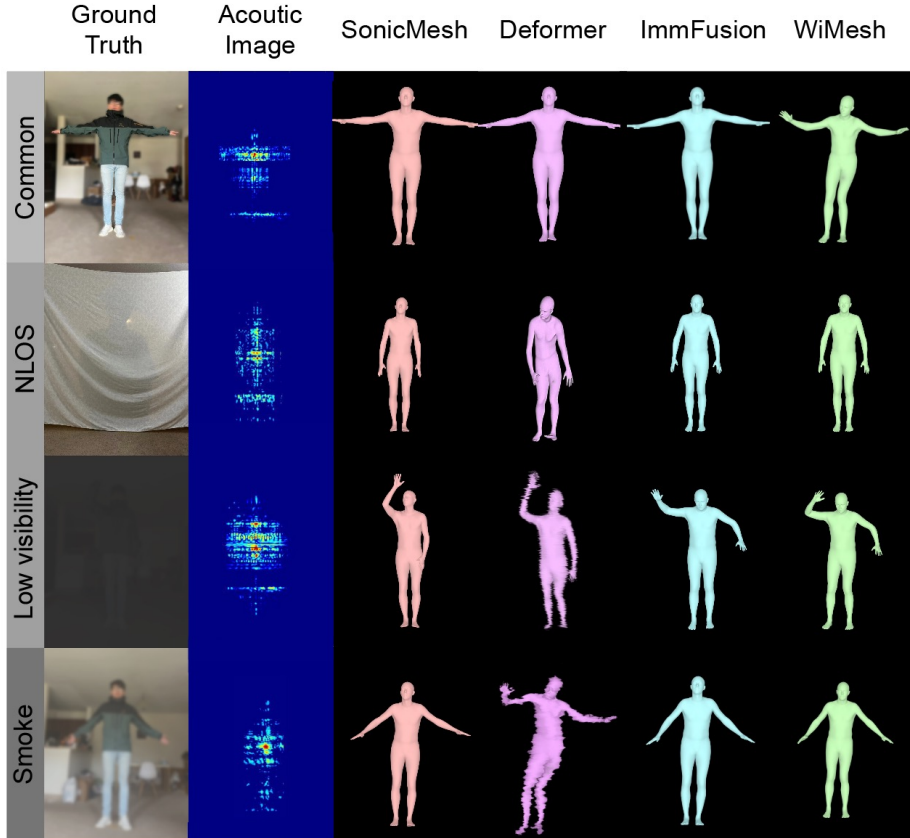


Figure 3. Qualitative results (compared with Deformer, ImmFusion, and WiMesh in common, NLOS, low visibility, and smoke scenes).

learning from both modalities. By preventing over-reliance on either modality during training, we can ensure the system maintains robust performance regardless of environmental conditions, effectively utilizing whichever signal provides the most reliable information in any given situation.

To ensure balanced learning across modalities, we implement a two-pronged approach. First, we employ modality masking, which randomly occludes either RGB or acoustic inputs during training. This forces the model to learn robust features from each modality independently, preventing over-reliance on any single input source. Second, we incorporate a Global Integrated Module (GIM), inspired by (Chen et al., 2023), which dynamically weights the contribution of each modality based on input quality. While modality masking ensures independent feature learning, GIM optimizes the fusion of these features by adaptively combining information according to the reliability of each source. Full details of the GIM architecture and training process can be found in Chen et al. (2023).

5. Experiments

This section provides a comprehensive evaluation of SonicMesh. We begin with an introduction to the dataset and implementation details (Sec. 5.1), along with the evaluation metrics used. We then present the overall performance results (Sec. 5.2) and benchmark comparisons (Sec. 5.3). Finally, we analyze failure cases in specific scenarios (Sec. 5.4). Together, these elements offer a thorough assessment of SonicMesh’s effectiveness in 3D HMR.

5.1. Dataset and implementation

Dataset Inspired by Chen et al. (2022), we developed a comprehensive dataset to evaluate SonicMesh’s performance. We collected data from 20 volunteers (10 males, 10 females) performing eight daily activities across four distinct environments: conference room, laboratory, corridor, and living room. To rigorously test SonicMesh’s robustness, we intentionally incorporated challenging conditions including poor lighting, occlusions, and non-line-of-sight (NLOS) scenarios. Throughout the data collection process, ground truth data was captured using a calibrated camera system.

The dataset’s design emphasizes diversity across multiple dimensions - from participant demographics and body types to movement patterns and environmental settings. This comprehensive coverage enables SonicMesh to learn generalizable features that transfer well to real-world applications, where varying conditions and user characteristics are common. We plan to open-source the dataset upon paper acceptance to support further research in this area.

Implementation Our training process employs two complementary loss functions, inspired by ImmFusion (Chen et al., 2023). The first, mean absolute error loss (\mathcal{L}_1), minimizes differences between predicted and ground truth positions. We specifically choose this loss for its robustness to outliers and stable gradients during optimization, enabling reliable reconstruction even in challenging cases. The second, our feature matching loss ($\mathcal{L}_{\text{match}}$, defined in (6)), ensures structural integrity by aligning predicted mesh points with ground truth positions - a crucial aspect for preserving detailed anatomical features. To optimize performance, we empirically determine the relative weights of these loss terms, carefully balancing reconstruction accuracy with training convergence speed. Complete implementation specifications, including loss weights and training parameters, are provided in Sec. C.

5.2. Overall performance

This section evaluates SonicMesh’s effectiveness in 3D human mesh reconstruction through a comprehensive comparison with state-of-the-art (SOTA) models.

Performance evaluation metrics We assess performance using three complementary metrics to ensure thorough evaluation:

The primary metrics are Per Vertex Error (PVE) and Mean Per Joint Position Error (MPJPE). PVE measures the Euclidean distance between predicted and ground truth vertices, quantifying our model’s ability to capture accurate body geometry. MPJPE complements this by calculating the average Euclidean distance between predicted and ground truth joint positions, specifically evaluating pose estimation accuracy.

To provide an even more comprehensive assessment, we also employ the shape error evaluation method from (Chen et al., 2022), which analyzes both shape accuracy and joint alignment. Together, these metrics enable us to evaluate the full spectrum of reconstruction quality, from overall body shape to specific joint positions.

Performance of SonicMesh We evaluated SonicMesh’s performance in HMR across various environments. Fig. 3 shows that our method closely matches the ground truth for

most samples. SonicMesh maintains high accuracy even under challenging conditions like poor lighting or smoke-induced occlusions, demonstrating its robustness.

Comparison with the SOTA models We evaluated SonicMesh against several state-of-the-art (SOTA) methods across multiple dimensions: accuracy, hardware requirements, and practical deployability. Qualitative comparisons across different scenarios (Fig 3) demonstrate that SonicMesh outperforms existing methods in challenging conditions. The Deformer (Yoshiyasu, 2023), which relies solely on visual data, performs poorly in extreme environments, while our method achieves higher accuracy compared to ImmFusion (Chen et al., 2023) and WiMesh (Wang et al., 2023). Quantitative evaluation (Table 1) reveals significant trade-offs among current approaches. mmWave-based methods (Xue et al., 2021; Chen et al., 2023) offer low-cost, low-power, privacy-protective solutions but require specialized sensors. RF-based methods (Zhao et al., 2019; Wang et al., 2023) provide high transmission rates and low power consumption but need specific WiFi antennas. RGB-based methods (Lin et al., 2021a; Yoshiyasu, 2023) excel in normal conditions but struggle with poor lighting, occlusions, and NLOS scenarios while raising privacy concerns. SonicMesh bridges these trade-offs by using commonly available microphones and speakers, enabling easy deployment on commercial devices like cellphones. While our method achieves slightly lower accuracy than RGB-based approaches under ideal conditions (average MPJPE and PVE of 6cm and 8cm respectively), it significantly outperforms existing methods in challenging environments, offering a more practical and versatile solution. The use of common audio hardware eliminates the need for specialized sensors while maintaining robust performance across diverse conditions.

5.3. Benchmark

We assess the influence of various factors on SonicMesh’s performance.

Ablation study As discussed in Sec. 4, our model enhances previous methods with a registration module and exploits the backbone information of acoustic images using Fast-CNN and GMM. We assess the importance of these enhancements by comparing SonicMesh’s performance with and without these modules, as shown in Table 2. The results indicate: with these two modules, our method achieves significant improvements in shape and pose metrics, demonstrating the effectiveness of these enhancements.

Occlusion We evaluate SonicMesh’s performance under occlusions made from various materials. Fig. 4a illustrates the influence of occlusions on HMR across different methods. For certain occlusions, such as plastic and paper, the

Table 1. Comparative analysis of SOTA models.

Method	Signal	Low Power	Low Cost	Implementation Simplicity	Preserves Privacy	Scenes								Average	
						Normal		Poor-light		Occlusion		NLOS			
						MPJPE (cm)	PVE (cm)	MPJPE (cm)	PVE (cm)	MPJPE (cm)	PVE (cm)	MPJPE (cm)	PVE (cm)	MPJPE (cm)	PVE (cm)
mmMesh (Xue et al., 2021)	mmWave	✓	✓	✗	✓	6.53	8.12	6.47	7.95	7.06	8.23	6.95	8.15	6.80	8.12
RF-Avatar (Zhao et al., 2019)	RF	✗	✗	✗	✓	7.05	8.92	7.13	9.03	7.07	9.15	7.26	9.21	7.13	9.07
WiMesh (Wang et al., 2023)	RF	✗	✗	✗	✓	6.41	7.10	6.43	7.09	6.34	7.21	6.57	7.43	6.50	7.21
ImmFusion (Chen et al., 2023)	mmWave	✓	✓	✗	✓	6.50	7.70	6.62	7.79	6.80	8.13	7.10	8.09	6.79	7.93
Graphormer (Lin et al., 2021a)	RGB	✗	✗	✓	✗	5.12	7.31	-	-	28.70	34.55	-	-	16.90	20.95
Deformer (Yoshiyasu, 2023)	RGB	✗	✗	✓	✗	4.48	6.14	-	-	27.50	31.23	-	-	16.10	18.70
SonicMesh	Acoustic	✓	✓	✓	✓	5.31	6.43	5.39	6.54	5.43	6.57	6.92	8.72	5.81	7.10

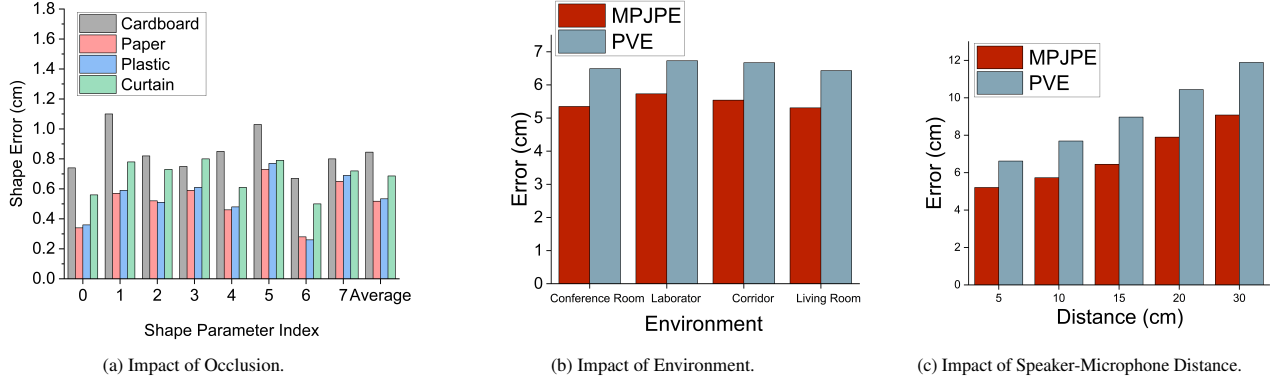


Figure 4. Influence of various factors.

Table 2. Ablation study

	PVE (cm)	MPJPE (cm)
SonicMesh	7.10	5.81
w/o Registration Module (RM)	9.39	7.87
w/o Fast-CNN + GMM + RM	13.63	10.58

average shape errors remain stable (e.g., 0.51 vs 0.53). However, occlusions with signal-absorbing properties increase shape error and materials like cardboard cause even higher errors due to their reflective nature.

Acoustic signal reflection distance We evaluate the impact of the distance between the speaker and microphone on SonicMesh’s performance by varying their separation, as illustrated in Fig. 4c. Tests were conducted at distances of 5cm, 10cm, 15cm, 20cm, and 30cm. The results indicate a decline in performance with increasing distance, primarily due to reduced signal strength, which hinders effective signal capture.

Different environments Our dataset includes four different environments: a living room (4m × 3m), a laboratory (20m × 10m), a corridor (3m × 20m), and a conference

room (5m × 7m). Each environment contains varying levels of furnishings, which introduce different degrees of multipath effects. We assessed the impact of these environmental differences and multipath effects on SonicMesh’s performance, as shown in Fig. 4b. The results across the four settings are relatively consistent, largely due to the effectiveness of the background subtraction technique used to mitigate multipath interference.

5.4. Failure cases

In real-world applications, SonicMesh may face certain limitations that result in failure cases. These include challenges such as detecting unusual body postures, managing scenarios with multiple targets in close proximity, or identifying targets behind obstacles. For instance, SonicMesh has difficulty recognizing subtle actions, such as tying shoes, due to limitations in its body mesh model. Additionally, when two targets are close together, their acoustic signals overlap in the captured image, which prevents the system from distinguishing between them and results in recognition failures. Furthermore, since acoustic signals cannot penetrate walls, SonicMesh is unable to perform HMR on targets that are located behind barriers.

6. Conclusion

In this paper, we introduce SonicMesh, the first method to combine acoustic and RGB images for 3D human mesh reconstruction. Our approach addresses fundamental limitations of traditional camera-based methods through two key technical innovations. First, we incorporate a registration module that aligns pixel feature embeddings from 2D images with 3D canonical feature embeddings, effectively addressing the depth ambiguity inherent in 2D-to-3D reconstruction. Second, we enhance the HRNet architecture to better process low-resolution acoustic images, enabling effective feature extraction despite the quality limitations of acoustic signals. Experimental results demonstrate that this dual-innovation approach enables SonicMesh to overcome longstanding challenges in 3D reconstruction. The system maintains robust performance across challenging scenarios where traditional methods fail, including non-line-of-sight (NLOS) conditions, poor lighting environments, and occluded scenes. By effectively combining the complementary strengths of acoustic and RGB modalities, SonicMesh represents a significant advance in reliable 3D human mesh reconstruction.

References

- Bai, X., Hu, Z., Zhu, X., Huang, Q., Chen, Y., Fu, H., and Tai, C.-L. Transfusion: Robust lidar-camera fusion for 3d object detection with transformers. In *2022 IEEE/CVF Conference on Computer Vision and Pattern Recognition (CVPR)*, pp. 1080–1089, New Orleans, LA, USA, 2022. IEEE. ISBN 978-1-6654-6947-0. doi: 10.1109/CVPR52688.2022.00116.
- Bijelic, M., Gruber, T., Mannan, F., Kraus, F., Ritter, W., Dietmayer, K., and Heide, F. Seeing through fog without seeing fog: Deep multimodal sensor fusion in unseen adverse weather. In *2020 IEEE/CVF Conference on Computer Vision and Pattern Recognition (CVPR)*, pp. 11679–11689, Seattle, WA, USA, 2020. IEEE. ISBN 978-1-7281-7169-2. doi: 10.1109/CVPR42600.2020.01170.
- Cai, C., Chen, Z., Pu, H., Ye, L., Hu, M., and Luo, J. Acute: acoustic thermometer empowered by a single smartphone. In *Proceedings of the 18th Conference on Embedded Networked Sensor Systems, SenSys '20*, pp. 28–41, New York, NY, USA, 11 2020. Association for Computing Machinery. ISBN 9781450375900. doi: 10.1145/3384419.3430714. URL <https://doi.org/10.1145/3384419.3430714>.
- Chen, A., Wang, X., Zhu, S., Li, Y., Chen, J., and Ye, Q. mmbody benchmark: 3d body reconstruction dataset and analysis for millimeter wave radar. In *Proceedings of the 30th ACM International Conference on Multimedia, MM '22*, pp. 3501–3510, New York, NY, USA, 10 2022. Association for Computing Machinery. ISBN 9781450392037. doi: 10.1145/3503161.3548262. URL <https://doi.org/10.1145/3503161.3548262>.
- Chen, A., Wang, X., Shi, K., Zhu, S., Fang, B., Chen, Y., Chen, J., Huo, Y., and Ye, Q. Immfusion: Robust mmwave-rgb fusion for 3d human body reconstruction in all weather conditions. In *2023 IEEE International Conference on Robotics and Automation (ICRA)*, pp. 2752–2758. IEEE, 2023.
- Chen, Y.-C., Li, G., Zhang, Q., Zhang, Q.-J., and Xia, X.-G. Motion compensation for airborne sar via parametric sparse representation. *IEEE Transactions on Geoscience and Remote Sensing*, 55:551–562, 2017. ISSN 1558-0644. doi: 10.1109/TGRS.2016.2611522.
- Fan, H., Yang, Y., and Kankanhalli, M. Point 4d transformer networks for spatio-temporal modeling in point cloud videos. In *2021 IEEE/CVF Conference on Computer Vision and Pattern Recognition (CVPR)*, pp. 14199–14208, Nashville, TN, USA, 2021. IEEE. ISBN 978-1-6654-4510-8. doi: 10.1109/CVPR46437.2021.01398.
- Fang, H., Xie, S., Tai, Y., and Lu, C. RMPE: regional multi-person pose estimation. In *IEEE International Conference on Computer Vision, ICCV 2017, Venice, Italy, October 22-29, 2017*, pp. 2353–2362. IEEE Computer Society, 2017. doi: 10.1109/ICCV.2017.256.
- Geng, J., Huang, D., and la Torre, F. D. Densepose from wifi. *Arxiv*, December 2022.
- Girshick, R. Fast r-cnn, 2015. URL <https://arxiv.org/abs/1504.08083>.
- Li, D., Liu, J., Lee, S. I., and Xiong, J. Fm-track: pushing the limits of contactless multi-target tracking using acoustic signals. In *Proceedings of the 18th Conference on Embedded Networked Sensor Systems, SenSys '20*, pp. 150–163, New York, NY, USA, 11 2020. Association for Computing Machinery. ISBN 9781450375900. doi: 10.1145/3384419.3430780. URL <https://doi.org/10.1145/3384419.3430780>.
- Li, Y., Yu, A. W., Meng, T., Caine, B., Ngiam, J., Peng, D., Shen, J., Lu, Y., Zhou, D., Le, Q. V., Yuille, A., and Tan, M. Deepfusion: Lidar-camera deep fusion for multi-modal 3d object detection. In *2022 IEEE/CVF Conference on Computer Vision and Pattern Recognition (CVPR)*, pp. 17161–17170, New Orleans, LA, USA, 2022. IEEE. ISBN 978-1-6654-6947-0. doi: 10.1109/CVPR52688.2022.01667.

- Liang, X., Wei, Z., Li, D., Xiong, J., and Gummeson, J. Sonar: Size and shape measurements using acoustic imaging. In *Proceedings of the Twenty-fifth International Symposium on Theory, Algorithmic Foundations, and Protocol Design for Mobile Networks and Mobile Computing*, MobiHoc '24, pp. 361–370, New York, NY, USA, 10 2024. Association for Computing Machinery. ISBN 9798400705212. doi: 10.1145/3641512.3686359. URL <https://doi.org/10.1145/3641512.3686359>.
- Lin, K., Wang, L., and Liu, Z. Mesh graphormer. In *2021 IEEE/CVF International Conference on Computer Vision (ICCV)*, pp. 12919–12928, 2021a. doi: 10.1109/ICCV48922.2021.01270.
- Lin, K., Wang, L., and Liu, Z. End-to-end human pose and mesh reconstruction with transformers. In *Proceedings of the IEEE/CVF conference on computer vision and pattern recognition*, pp. 1954–1963, 2021b.
- Loper, M., Mahmood, N., Romero, J., Pons-Moll, G., and Black, M. J. Smpl: A skinned multi-person linear model. In *Seminal Graphics Papers: Pushing the Boundaries, Volume 2*, pp. 851–866. ACM, 2023.
- Mahafza, B. R. *Radar systems analysis and design using MATLAB*. Boca Raton, FL: CRC Press, 3rd ed. edition, 2013. ISBN 978-1-4398-8495-9; 978-1-58488-854-3.
- Mao, W., He, J., and Qiu, L. Cat: High-precision acoustic motion tracking. In *Proceedings of the 22nd Annual International Conference on Mobile Computing and Networking*, MobiCom '16, pp. 69–81, New York, NY, USA, 2016. Association for Computing Machinery. ISBN 9781450342261. doi: 10.1145/2973750.2973755. URL <https://doi.org/10.1145/2973750.2973755>.
- Mao, W., Zhang, Z., Qiu, L., He, J., Cui, Y., and Yun, S. Indoor follow me drone. In *Proceedings of the 15th Annual International Conference on Mobile Systems, Applications, and Services*, MobiSys '17, pp. 345–358, New York, NY, USA, 6 2017. Association for Computing Machinery. ISBN 9781450349284. doi: 10.1145/3081333.3081362. URL <https://doi.org/10.1145/3081333.3081362>.
- Mao, W., Wang, M., and Qiu, L. Aim: Acoustic imaging on a mobile. In *Proceedings of the 16th Annual International Conference on Mobile Systems, Applications, and Services*, MobiSys '18, pp. 468–481, New York, NY, USA, 6 2018. Association for Computing Machinery. ISBN 9781450357203. doi: 10.1145/3210240.3210325. URL <https://doi.org/10.1145/3210240.3210325>.
- Moro, G., Bin, A., Jack, R. H., Heinrichs, C., and Mcpherson, A. Making high-performance embedded instruments with bela and pure data. In *Queen Mary University of London*, 2016. URL <https://api.semanticscholar.org/CorpusID:3481420>.
- Pavlakos, G., Choutas, V., Ghorbani, N., Bolkart, T., Osman, A. A., Tzionas, D., and Black, M. J. Expressive body capture: 3d hands, face, and body from a single image. In *2019 IEEE/CVF Conference on Computer Vision and Pattern Recognition (CVPR)*, pp. 10967–10977, Long Beach, CA, USA, 2019. IEEE. ISBN 978-1-7281-3294-5. doi: 10.1109/CVPR.2019.01123.
- Qi, C. R., Yi, L., Su, H., and Guibas, L. J. Pointnet++: deep hierarchical feature learning on point sets in a metric space. In *Proceedings of the 31st International Conference on Neural Information Processing Systems, NIPS'17*, pp. 5105–5114, Red Hook, NY, USA, 2017. Curran Associates Inc. ISBN 9781510860964.
- Qian, K., Wu, C., Xiao, F., Zheng, Y., Zhang, Y., Yang, Z., and Liu, Y. Acousticcardiogram: Monitoring heartbeats using acoustic signals on smart devices. In *IEEE INFOCOM 2018 - IEEE Conference on Computer Communications*, pp. 1574–1582, 2018. doi: 10.1109/INFOCOM.2018.8485978.
- Ryselis, K., Petkus, T., Blažauskas, T., Maskeliūnas, R., and Damaševičius, R. Multiple kinect based system to monitor and analyze key performance indicators of physical training. *Human-centric Computing and Information Sciences*, 10(1), December 2020. ISSN 2192-1962. doi: 10.1186/s13673-020-00256-4.
- Shibata, Y., Kawashima, Y., Isogawa, M., Irie, G., Kimura, A., and Aoki, Y. Listening human behavior: 3d human pose estimation with acoustic signals. In *Proceedings of the IEEE/CVF Conference on Computer Vision and Pattern Recognition (CVPR)*, pp. 13323–13332, June 2023.
- Sun, K., Xiao, B., Liu, D., and Wang, J. Deep high-resolution representation learning for human pose estimation. In *2019 IEEE/CVF Conference on Computer Vision and Pattern Recognition (CVPR)*, pp. 5686–5696, Long Beach, CA, USA, 2019. IEEE. ISBN 978-1-7281-3294-5. doi: 10.1109/CVPR.2019.00584.
- Tang, X., Wang, T., and Fu, C. Towards accurate alignment in real-time 3d hand-mesh reconstruction. In *2021 IEEE/CVF International Conference on Computer Vision, ICCV 2021, Montreal, QC, Canada, October 10-17, 2021*, pp. 11678–11687. IEEE, 2021. doi: 10.1109/ICCV48922.2021.01149.
- Wang, P., Jiang, R., and Liu, C. Amaging: Acoustic hand imaging for self-adaptive gesture recognition. In

- IEEE INFOCOM 2022 - IEEE Conference on Computer Communications*, pp. 80–89, London, United Kingdom, 2022a. IEEE. ISBN 978-1-6654-5823-8. doi: 10.1109/INFOCOM48880.2022.9796906.
- Wang, P., Jiang, R., and Liu, C. Amaging: Acoustic hand imaging for self-adaptive gesture recognition. In *IEEE INFOCOM 2022-IEEE Conference on Computer Communications*, pp. 80–89. IEEE, 2022b.
- Wang, Y., Chen, X., Cao, L., Huang, W., Sun, F., and Wang, Y. Multimodal token fusion for vision transformers. In *2022 IEEE/CVF Conference on Computer Vision and Pattern Recognition (CVPR)*, pp. 12176–12185, New Orleans, LA, USA, 2022c. IEEE. ISBN 978-1-6654-6947-0. doi: 10.1109/CVPR52688.2022.01187.
- Wang, Y., Ye, T., Cao, L., Huang, W., Sun, F., He, F., and Tao, D. Bridged transformer for vision and point cloud 3d object detection. In *2022 IEEE/CVF Conference on Computer Vision and Pattern Recognition (CVPR)*, pp. 12104–12113, New Orleans, LA, USA, 2022d. IEEE. ISBN 978-1-6654-6947-0. doi: 10.1109/CVPR52688.2022.01180.
- Wang, Y., Ren, Y., Chen, Y., and Yang, J. Wi-mesh: A wifi vision-based approach for 3d human mesh construction. In *Proceedings of the 20th ACM Conference on Embedded Networked Sensor Systems, SenSys '22*, pp. 362–376, New York, NY, USA, 1 2023. Association for Computing Machinery. ISBN 9781450398862. doi: 10.1145/3560905.3568536. URL <https://doi.org/10.1145/3560905.3568536>.
- Xue, H., Ju, Y., Miao, C., Wang, Y., Wang, S., Zhang, A., and Su, L. mmmesh: towards 3d real-time dynamic human mesh construction using millimeter-wave. In *Proceedings of the 19th Annual International Conference on Mobile Systems, Applications, and Services, MobiSys '21*, pp. 269–282, New York, NY, USA, 6 2021. Association for Computing Machinery. ISBN 9781450384438. doi: 10.1145/3458864.3467679. URL <https://doi.org/10.1145/3458864.3467679>.
- Yang, G., Vo, M., Neverova, N., Ramanan, D., Vedaldi, A., and Joo, H. Banmo: Building animatable 3d neural models from many casual videos. In *2022 IEEE/CVF Conference on Computer Vision and Pattern Recognition (CVPR)*, pp. 2853–2863, New Orleans, LA, USA, 2022a. IEEE. ISBN 978-1-6654-6947-0. doi: 10.1109/CVPR52688.2022.00288.
- Yang, Z., Fan, X., Isler, V., and Park, H. S. Posekernellifter: Metric lifting of 3d human pose using sound. In *2022 IEEE/CVF Conference on Computer Vision and Pattern Recognition (CVPR)*, pp. 13169–13179, New Orleans, LA, USA, 2022b. IEEE. ISBN 978-1-6654-6947-0. doi: 10.1109/CVPR52688.2022.01283.
- Yoshiyasu, Y. Deformable mesh transformer for 3d human mesh recovery. In *2023 IEEE/CVF Conference on Computer Vision and Pattern Recognition (CVPR)*, pp. 17006–17015, Vancouver, BC, Canada, 2023. IEEE. ISBN 978-8-3503-0130-4. doi: 10.1109/CVPR52729.2023.01631.
- Zhao, M., Liu, Y., Raghu, A., Zhao, H., Li, T., Torralba, A., and Katabi, D. Through-wall human mesh recovery using radio signals. In *2019 IEEE/CVF International Conference on Computer Vision (ICCV)*, pp. 10112–10121, Seoul, Korea (South), 2019. IEEE. ISBN 978-1-7281-4804-5. doi: 10.1109/ICCV.2019.01021.
- Zheng, J., Shi, X., Gorban, A. N., Mao, J., Song, Y., Qi, C. R., Liu, T., Chari, V., Cornman, A., Zhou, Y., Li, C., and Anguelov, D. Multi-modal 3d human pose estimation with 2d weak supervision in autonomous driving. In *IEEE/CVF Conference on Computer Vision and Pattern Recognition Workshops, CVPR Workshops 2022, New Orleans, LA, USA, June 19-20, 2022*, pp. 4477–4486. IEEE, 2022. doi: 10.1109/CVPRW56347.2022.00494.

A. The principle of images generated by acoustic signals

The contents in this section are adapted from Liang et al. (2024). To maintain consistency, we include several key elements from Liang et al. (2024) here. For a comprehensive overview of the experimental results, please refer to Liang et al. (2024).

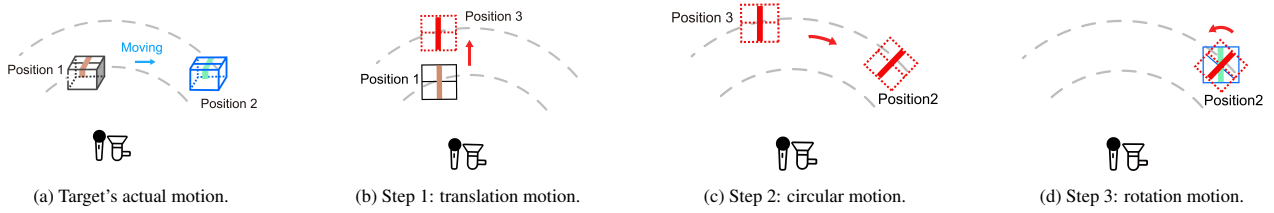


Figure 5. The target's actual motion can be decomposed into three steps: (a) translation motion, (b) circular motion, and (c) rotation motion.

A.1. Why acoustic images are low-resolution

The differences in image formation mechanisms between RGB and acoustic imaging systems create significant challenges for pose identification algorithms. While RGB images are formed through light reflection and capture rich visual details, including color, texture, and sharp edges, as shown in (Ground Truth column of) Fig. 3, acoustic images are generated through sound wave reflections. As shown in (Acoustic Image column of) Fig. 3, acoustic images exhibit low resolution, reduced contrast, and more diffuse boundaries due to the fundamental physics of sound wave propagation and reflection.

A.2. The principle of ISAR

Inverse Synthetic Aperture Radar (ISAR) is commonly employed in military applications to identify the shapes of moving targets, such as ships. Unlike motion tracking systems that consider the target as a single point, ISAR regards the target as an array of scatter points. ISAR imaging converts the target's translational motion into rotational motion, allowing for the capture of reflected signals from various perspectives around the target.

As shown in Fig.5a, consider a target moving from Position 1 to Position 2. This movement is illustrated in three stages in Fig.5b-5d. First, the target moves radially from Position 1 to Position 3 (Fig.5b), resulting in additional propagation delays in the signals reflected from each scatter point. These delays introduce image distortion, which is corrected using our echo alignment technique. In the second stage, the target moves along a circular path centered on the imaging device, from Position 3 to Position 2 (Fig.5c), without affecting propagation delays or the final image outcome. In the final stage, the target rotates around its geometric center by a specific angle (Fig. 5d), aligning with the azimuth angle traced during its actual movement.

A.3. The Basics of Chirp Signal

A speaker emits a series of chirp signals with frequencies that linearly sweep over time, as shown in Fig. 6a. The frequency of each chirp ranges from $f_c - \frac{B}{2}$ to $f_c + \frac{B}{2}$, where f_c is the carrier frequency and B is the bandwidth. Each chirp lasts for a duration T_c , followed by a pause, T_e , to allow all echoes from one chirp to return before the next chirp is emitted. Each chirp can be mathematically expressed as

$$s(t) = \text{rect} \left[\frac{t}{T_c} \right] \cos \left(2\pi \left(f_c t + \frac{k}{2} t^2 \right) \right), \quad (10)$$

where $k = \frac{B}{T_c}$ is the slope of the chirp. The term $\text{rect}[\cdot]$ refers to the rectangle window function, which is defined as

$$\text{rect}[\cdot] = \begin{cases} 1 & |\cdot| \leq 0.5 \\ 0 & |\cdot| \geq 0.5. \end{cases} \quad (11)$$

The total duration of each chirp cycle, including the pause, is $T = T_c + T_e$. The transmitted chirp signal is reflected by the target and received by a microphone, creating an echo. The time delay ($\Delta\tau$) of the echo is typically calculated by correlating

the transmitted chirp signal with the received echo (Mahafza, 2013). Using this time delay, the distance D between the target and the device can be determined by:

$$D = \frac{\Delta\tau \times v_s}{2}, \quad (12)$$

where v_s is the sound propagation speed in the air.



Figure 6. The signal illustration for imaging.

A.4. Signal Model for Imaging

The received echo signals are organized into a profile matrix for imaging, as illustrated in Fig. 6b. This matrix arranges M samples per column with N consecutive collected profiles to construct the image. Then we apply the Hilbert transform to the echo signals, followed by dechirping each column to extract the intermediate frequency (IF) signal matrix. Subsequently, a 2-D Fast Fourier Transform (FFT) is performed on the IF signal matrix along both the range and azimuth dimensions. This step effectively maps each scatter point in physical space to a corresponding pixel in the image space, I , where a scatter point p is identified by a peak at position (p_r, p_a) in the 2-D image space, which can be represented as

$$I(i_a, i_r) = A \operatorname{sinc} \left[\frac{2kT}{v_s} (i_r - p_r) \right] \times \operatorname{sinc} \left[\frac{2\theta}{\lambda} (i_a - p_a) \right], \quad (13)$$

where A is a constant related to the amplitude and chirp duration, v_s is the sound speed, λ is the wavelength, θ is the angle that the target rotates during the imaging process, i_r and i_a are the indexes along the range dimension and azimuth dimension, respectively.

B. Architecture of SonicMesh

B.1. Perserving anatomy

Separate CNNs process these enriched local features to generate global features, offering a complete scene view. The CNNs are designed to preserve and highlight the properties of both acoustic and RGB data, ensuring accurate human mesh reconstruction.

These global features are fused into a single global feature vector, incorporating the SMLP-X template (Pavlakos et al., 2019; Chen et al., 2023). This fusion leverages structural and depth cues from acoustic data and color and texture details from RGB data, creating a unified representation.

The integrated features are tokenized and input into a multi-layer Fusion Transformer Module, which dynamically merges data from both modalities. The module directly regresses the coordinates of 3D human joints and coarse mesh vertices, using self-attention mechanisms to prioritize relevant features.

Finally, Multi-Layer Perceptrons (MLPs) refine these coarse vertices into detailed SMPL-X (Pavlakos et al., 2019) mesh vertices. We choose SMPL-X for its comprehensive representation of the human body, capturing facial expressions and hand poses critical for virtual reality and medical applications.

The MLPs act as a final refinement step, enhancing the precision of the 3D mesh by correcting minor errors and adding finer

details to the vertices. This ensures that the model can accurately capture subtle anatomical features and expressions. The use of SMPL-X in this context provides several advantages:

- **Comprehensive Coverage:** SMPL-X includes detailed models of the body, face, and hands, allowing for a full-body representation of detailed human models.
- **Consistency Across Parts:** By integrating all parts of the human form into a single model, SMPL-X ensures consistency in movement and appearance, which is crucial for creating realistic reconstruction of human mesh.

SMPL-X requires precise joint positions and body part relationships to generate accurate meshes, but the template itself cannot guide the extraction of these structural features from multimodal inputs. Current methods (Chen et al., 2023) attempt to bridge this gap using generic backbones to extract and combine features from different modalities (Qi et al., 2017; Fan et al., 2021; Wang et al., 2022a). However, these approaches face three critical limitations: (1) they cannot effectively align SMPL-X’s predefined joint hierarchy with features extracted from 2D observations, (2) they lose spatial relationships when projecting features between 2D and 3D spaces, and (3) they lack mechanisms to verify whether extracted features conform to SMPL-X’s anatomical constraints.

B.2. Local and global features

We separate features to two distinct scales:

- *Local Features:* Capture fine-grained anatomical details such as:
 - Joint articulations (e.g., knee and elbow bend angles)
 - Body part boundaries and contours
 - Local surface deformations
 - Individual limb positions and orientations
- *Global Features:* Represent overall body configuration including:
 - Full-body pose and orientation
 - Inter-limb spatial relationships
 - Body proportions and scale
 - Overall skeletal structure

B.3. Why soft argmax

The use of soft argmax helps efficiently align the 2D and 3D features by providing a smooth, differentiable approximation of the argmax function. This approximation allows gradients to flow back through the network, facilitating effective learning. The soft argmax operates by first calculating the cosine similarity between each 2D joint feature vector $\psi^a(\mathbf{k}_j^a)$ and the feature vectors of sampled 3D points $\psi(\mathbf{K})$ in \mathbf{V}^* . The resulting similarities indicate how closely each 2D feature aligns with potential 3D points. The softmax function then normalizes these similarity scores, converting them into weights that sum to one. These weights represent the likelihood that each 3D point corresponds to the 2D joint. By weighting the 3D points \mathbf{K} in \mathbf{V}^* with these normalized scores, we effectively compute a weighted average position, $\tilde{\mathbf{K}}_j^*$, that represents the most likely 3D location corresponding to the 2D joint. This method ensures precise alignment of 2D joints with their corresponding 3D locations, providing accurate spatial mapping across dimensions.

C. Implementation details

In this section, we will introduce the detail of our implementation.

C.1. Devices

All models are implemented in Pytorch and trained on an NVIDIA GeForce RTX 4090. Each network is trained from scratch for 50 epochs using an Adam optimizer with an initial learning rate of 0.001.



Figure 7. The 16 critical joints used in our registration module. The front view shows the primary joints (1-13), including the head, shoulders, elbows, wrists, hips, knees, and ankles. Side view highlights the three additional spine joints (14-16) that help maintain proper posture estimation.

C.2. Human joints

Fig. 7 shows the 16 human joints we considered.

C.3. Acoustic device and configuration

We implement our proof-of-concept system using a commodity device: a Bela (Moro et al., 2016) platform. Signal processing and analysis are carried out using MATLAB.

Bela Platform: The Bela (Moro et al., 2016) platform is favored in acoustic sensing research for its versatility in supporting various microphone and speaker configurations. We equipped the Bela with a PUI Audio AS03104MR-N50-R speaker for signal transmission and a SparkFun BOB-18011 MEMS microphone for signal reception.

Acoustic Signals: To avoid interference from environmental noise, which typically falls below 16 kHz (Liang et al., 2024), we configure our system to sweep frequencies from 18 kHz to 22 kHz . The duration of each chirp is set as 1 ms , and the empty duration is set as 5 ms .

C.4. Dataset

For our dataset of acoustic images, we defined eight common daily actions: standing, arms spreading, raising one hand, raising both hands, arms spread diagonally upward, arms stretched downward, arms extended straight up, and raising one arm to the side. For each action, data was collected from 20 volunteers (10 male and 10 female) with 100 samples per action. We introduced 3 challenges—poor lighting, occlusions, and smoke (to simulate NLOS)—each representing 25% of the total collected data. Fig 8 shows these poses and their corresponding generated acoustic images. We used a calibrated Samsung S24 as the camera system to capture RGB images, which serve as the ground truth in our dataset.

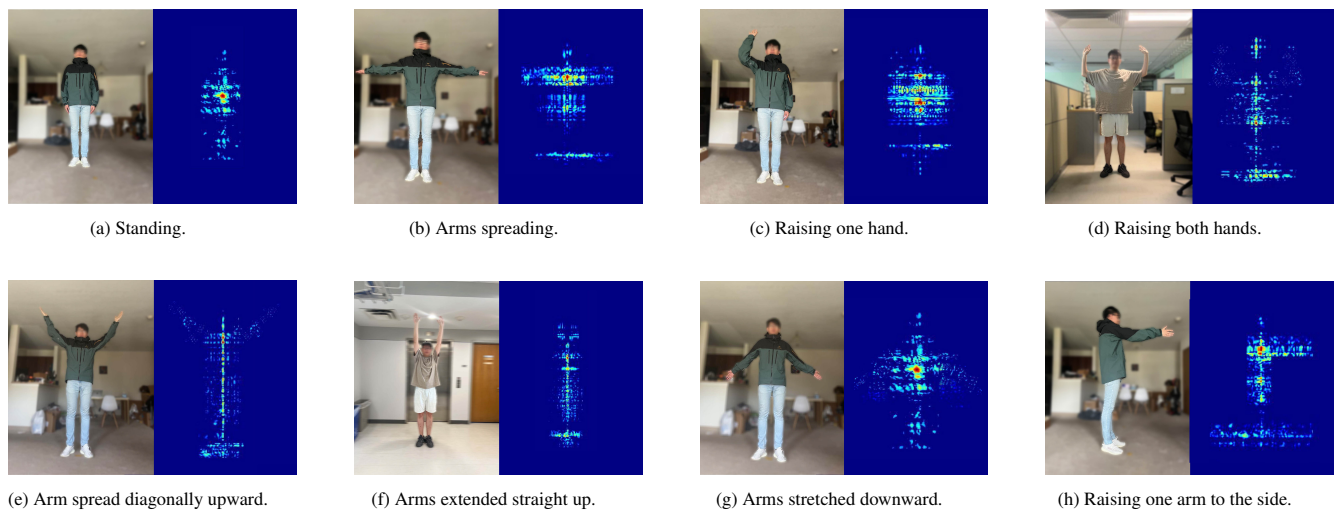


Figure 8. The signal illustration for imaging.